

# Optical single photon detection in micron-scaled NbN bridges

Y. Korneeva

*Physics Department, Moscow State University of Education, Moscow, Russia\**

D.Yu. Vodolazov

*Institute for Physics of Microstructures, Russian Academy of Sciences, Nizhny Novgorod, GSP-105, Russia  
and Physics Department, Moscow State University of Education, Moscow, Russia*

A. V. Semenov

*Physics Department, Moscow State University of Education, Moscow, Russia  
and Moscow Institute of Physics and Technology (State University), Moscow, Russia*

I. Florya and N. Simonov

*Physics Department, Moscow State University of Education, Moscow, Russia*

E. Baeva

*Higher School of Economics National Research University, Moscow, Russia  
and Physics Department, Moscow State University of Education, Moscow, Russia*

A.A. Korneev

*Physics Department, Moscow State University of Education, Moscow, Russia,  
Moscow Institute of Physics and Technology (State University), Moscow, Russia  
and Higher School of Economics National Research University, Moscow, Russia*

G.N. Goltsman

*Physics Department, Moscow State University of Education, Moscow, Russia  
and Higher School of Economics National Research University, Moscow, Russia*

T.M. Klapwijk

*Physics Department, Moscow State University of Education, Moscow, Russia  
and Kavli Institute of Nanoscience, Delft University of Technology, The Netherlands*

(Dated: February 9, 2018)

We demonstrate experimentally that single photon detection can be achieved in micron-wide NbN bridges, with widths ranging from  $0.53\ \mu\text{m}$  to  $5.15\ \mu\text{m}$  and for photon-wavelengths from 408 nm to 1550 nm. The microbridges are biased with a dc current close to the experimental critical current, which is estimated to be about 50% of the theoretically expected depairing current. These results offer an alternative to the standard superconducting single-photon detectors (SSPDs), based on nanometer scale nanowires implemented in a long meandering structure. The results are consistent with improved theoretical modelling based on the theory of non-equilibrium superconductivity including the vortex-assisted mechanism of initial dissipation.

## I. INTRODUCTION

The present superconducting nanowire single photon detectors (SSPD's) are based on long meandering superconducting strips with a width in the range of 50 to 150 nm [1]. It has been empirically found that the use of wider strips leads either to the loss of the single photon nature of the response or to a rather small detection efficiency [2, 3]. This result is in line with the initial interpretation of this type of detector [4, 5], in which it was understood that the width of the supercurrent-carrying strip should be comparable to the diameter,  $D$ ,

of the normal hot spot (a region where the superconducting state is suppressed), due to the absorption of the photon. If the strip is biased near its experimentally determined critical current, the emergence of the hot-spot forces a redistribution of the supercurrent, leading to a locally enhanced supercurrent-density, triggering the switch to the resistive state. Using simple estimates, based on the conservation of energy and typical parameters for niobium-nitride (NbN), given the energy of an optical photon leads to  $D \sim 40\ \text{nm}$  for the expected size of the normal hot spot [6].

This geometrical mechanism to exceed the critical current-density, has initiated a more thorough analysis of the conditions of the superconducting strips under current-bias by Zotova and Vodolazov [7, 8]. They consider a superconducting strip, biased sufficiently close to

---

\* korneeva@rplab.ru

the intrinsic *depairing* current  $I_{dep}$ . Then a small amount of energy can switch the current-carrying superconductor to a resistive state, with the needed energy going to zero when  $I$  approaches  $I_{dep}$ . The only requirement for the width of the strip is that it should be smaller than the Pearl penetration depth  $\Lambda = 2\lambda^2/d$  (with  $\lambda$  the London penetration depth for a dirty superconductor and  $d$  the thickness of the strip). Under these conditions the supercurrent will be uniform across the width, whereas for wider strips the supercurrent will be distributed non-uniformly. For a typical NbN films with a thickness about 5 nm and  $\lambda \sim 470$  nm [9] one obtains  $\Lambda \simeq 90$   $\mu\text{m}$ .

Using the microscopic theory for superconductivity it was shown in Refs. 7, 8, that if such a strip with a uniform supercurrent  $I$  can be biased at  $I \gtrsim 0.5 - 0.7I_{dep}$  the superconducting state becomes unstable in response to relatively small additions of energy in the form of a localized disturbance, loosely called a 'hot spot'. Its specific nature in terms of the microscopic theory of non-equilibrium superconductivity has not yet been worked out. It is considered to be a localized nonequilibrium distribution over the energies and with at least a depressed local energy gap initially surrounded by an equilibrium superconductor. The dynamics of such an 'impact crater' in the superconducting film will depend on the materials.

In previous work this process was mostly described by what we label as a 'geometric-hot-spot-model'. The essential feature of this approach is that the supercurrent, initially carried over the full width  $w$  of the supercurrent in the wire is pushed to a more narrow part, excluding the 'hot' part with a diameter  $d$ . This increased current density then may exceed the critical current density initiating a transition to a voltage-carrying state. To optimize the efficiency of detection the wire should be of the order of the size  $d$  of the hot spot in the superconductor created by the absorbed photon. This geometric hot spot model is often used for a qualitative discussions and has been mostly leading the technological development.

More recently, the microscopic approach has emerged including the use of nonequilibrium superconductivity. In this approach the phase-coherence of the superfluid flow is fully taken into account, as well as the emergence of resistivity in the superconductor by the creation of vortices. In order to make a clear distinction with previous approaches we call this the 'photon-generated superconducting vortex model'. The theory states that the efficiency of the photon-detection is not determined by the geometry, as long as the initial current-density is uniform and close to the critical pair-breaking current. The requirement for uniformity of the current density is given in a previous paragraph. If the superconducting wire can be biased close to the critical pair-breaking current, all photons will be detected, wherever they hit the wire, because all of them create a sufficient disturbance to trigger a *local* excess of the critical current density, initiating the creation of vortex-anti-vortex pairs. In the film vortex-antivortex pairs will be created inside the hot spot (if it is located far from the edge of the strip) or by vortex

entry into the strip (if the hot spot is located close to the edge). The motion of a vortex and/or anti-vortex due to the Lorentz force leads to a voltage in the superconductor and eventually to the appearance of a normal domain [8]. Rather than assuming a fully normal hot spot this model takes into account the resistive properties of the superconducting state due to vortex-movement, with details determining the full dynamics.

In order to build experimentally on a model based on current densities close to the critical pair-breaking current one needs to determine whether the observed critical current is determined by intrinsic or extrinsic properties, such as material imperfections. The commonly used material for single photon-detection is NbN with a thickness of about 5 nanometer, chosen because of its fast electron-phonon relaxation including phonon-escape to the substrate. However, such films have a fairly high resistivity, a low diffusion constant, and a high resistance per square in the order of 800  $\Omega$ , which implies that they have an intrinsic tendency to become electronically inhomogeneous with a spatially fluctuating superconducting energy gap [10, 11], which may worsen due to material imperfections. Therefore, it is to be expected that the critical current for a long superconducting wire is determined by the weakest spot, which statistically will be the lowest value of the energy gap along the wire. Secondly, in order to know the value of the critical depairing current one has to rely on a quantitative estimate based on measured parameters, and preferably on a comparison with the functional dependence, such as carried out for aluminium by Romijn et al [12]. Relatively high critical current densities have been reported recently by Charaev et al [13], although in more narrow strips larger values have been reported [3, 14]. Nevertheless, the maximally reachable value is not known and, given the expected inhomogeneities, may vary. Instead we have decided to work with relatively short microbridges and vary the width, to minimize the risks of hitting a too low critical current while expecting a reasonably uniform current density.

In this work we report on our findings that relatively wide NbN bridges with widths in the range of 0.53  $\mu\text{m}$  to 5.15  $\mu\text{m}$  are able to detect single photons of wavelengths from 408 nm to 1550 nm. We determine the Internal Detection Efficiency,  $IDE$ , the detection efficiency normalized to the absorption, for different bias currents  $I$ , and find that it reaches value of tens of percents near the experimental critical current  $I_c$ . From the experimental data we distinguish two regimes. *Regime I* in which for increasing current a sharp increase in  $IDE$  is observed, analogous to the conventional meanderlike SSPDs. It is followed by a much slower increase of the  $IDE$  upon approaching  $I_c$ , which we label *Regime II*. We attribute *Regime I* to fluctuation assisted photon detection with the slope of the  $IDE$  as a function of current  $I$  comparable to the slope of the number of dark counts with the bias current. The *Regime II* we attribute to deterministic photon counting as described theoretically by Zotova and Vodolazov [15]. We are able to explain quantita-

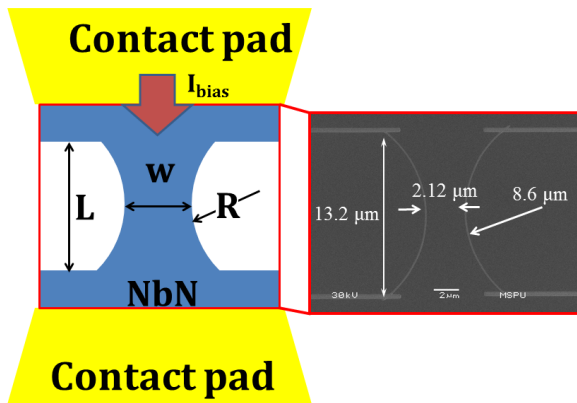


FIG. 1. Drawing of a typical NbN constriction-type bridge with a scanning electron microscope (SEM) image of one of the bridges with indicated dimensions (Sample *C* in Table I). The contacts on top of the NbN film are made of gold (Au). All bridges have edges designed as a segment of a circle with radius  $8.6 \mu\text{m}$ .

tively the dependence of the *IDE* on the current  $I$  in *Regime II* for the short wavelengths, taking into account the actual geometry of our samples. We argue that in this parameter-range we observe an *IDE* close to unity.

Our findings offer a new route towards superconducting single photon detectors with a short dead time, a few hundreds of picoseconds, because of the relatively small kinetic inductance of short superconducting bridges in comparison to the conventional superconducting meanders [1]. Additionally, our results provide support for the relevance of the vortex-assisted contribution to photon detection as proposed by one of the authors [8].

## II. SAMPLES AND CHARACTERIZATION

Our samples are planar constriction-type microbridges as shown in Fig. 1. They are made from reactively sputtered NbN films with a thickness, determined from a calibrated sputter rate and the sputter time, of  $5.8 \text{ nm}$ . The width  $w$  of the bridges at the narrowest point was varied from  $0.53 \mu\text{m}$  to  $5.15 \mu\text{m}$ . The constriction-type topology was chosen to prevent current crowding effects [16] and to maximize the chance to reach in the experiments the critical pair-breaking current. Note that given the properties of the NbN films the constrictions are much larger in length and width than the coherence length. Therefore, it is assumed that the wider part, with the lower current density does not lead to an enhancement of the critical pair-breaking current in contrast to the case treated by Aslamazov and Larkin [17] because of the short coherence length in NbN [18]. The parameters of the studied devices are summarized in Table I. The de-

tails of the fabrication process are presented in Appendix A.

The experimentally observed critical current densities  $j_c$  for two different temperatures  $T=4.2 \text{ K}$  and  $T=1.7 \text{ K}$ . In Table I these results are listed for temperature  $T=4.2 \text{ K}$ . Obviously, there is some scatter in the values of the critical temperature as well as in the critical current density. It indicates that there is some uncontrolled variation from sample to sample, although the samples are from the same film. This may be caused by the metallurgy resulting from the deposition-conditions but it may also be intrinsic due to the competition between localisation in this low diffusivity material and superconductivity. For a material like NbN the experimental values in this experimental geometry are reassuringly close to the theoretical values. Since these relatively wide samples have impractically high critical currents we connect a  $3 \Omega$  shunt resistor in parallel to the sample to prevent latching and to enable a spontaneous return to the superconducting state. Although not expected, this leads to different increases of experimentally observed critical currents when the shunt is connected. In Fig. 2(a) we show current-voltage characteristics for Sample *C* without (red curve) and with the  $3 \Omega$  shunt resistor (blue curve) with different critical currents (point A and point B, respectively). A similar observation has been reported and discussed previously by Brenner et al [19]. In our measurements this can be attributed, at least in part, to division of the current between the chip with superconducting bridge and the shunt: the branch with superconducting bridge contains also normal resistance, of order of a few tenths of Ohms, because this is a two-point measurement. Of course, the quantity of interest is a supercurrent, *i.e.* the current flowing through the sample; hence, we use the measured current with the shunt only as a value to plot the data.

We assume that the theoretical depairing currents can be described by the expression derived for clean superconductors by Bardeen [20]. It deviates by less than 3% from the results of the microscopic calculations for dirty superconductors, and which have been compared to experiments on aluminium by Romijn et al [12]):

$$I_{dep}(T) = I_{dep}(0) \left[ 1 - \left( \frac{T}{T_c} \right)^2 \right]^{3/2} \quad (1)$$

with the prefactor  $I_{dep}(0)$ , calculated from Eq. 31 in Clem et al [21]:

$$I_{dep}(0) = 0.74 \frac{w [\Delta(0)]^{3/2}}{e R_s \sqrt{\hbar D}}, \quad (2)$$

Here,  $\Delta(0)$  is the superconducting energy gap at 0 K,  $e$  is the electron charge,  $R_s$  is the resistance per square,  $D$  is the diffusivity. Strictly speaking Eqs.(1,2) are quantitatively valid for moderately dirty superconductors with  $k_F l \gg 1$  ( $k_F$  is the Fermi wavevector and  $l$  is the mean free path for elastic scattering). We also assume the BCS-ratio of  $\Delta(0)/k_B T_c \approx 1.76$ .

TABLE I. Parameters of the studied samples for temperature  $T=4.2$  K. Width of the bridge  $w$  is at the neck,  $T_c$  is the critical temperature determined from the midpoint of the resistive transition,  $\rho(20K)$  is resistivity at  $T=20$  K,  $j_c$  and  $j_c^{sh}$  are the critical current densities measured without and with a shunt resistor,  $j_{dep}$  is the calculated depairing current at the indicated temperature, using  $j_{dep}(0)$  the calculated critical depairing current at  $T = 0$  following from Eq.2 The variation in the calculated values are due to the variations in resistance per square determined for each sample. The diffusion constant  $D$  is kept constant.

Sample ID	width $\mu\text{m}$	$T_c$ K	$\rho(20K)$ $\mu\Omega \cdot \text{cm}$	$j_c(4.2K)$ $\text{A}/\text{cm}^2$	$j_c^{sh}(4.2K)$ $\text{A}/\text{cm}^2$	$j_{dep}(4.2K)$ $\text{A}/\text{cm}^2$	$j_{dep}(0)$ $\text{A}/\text{cm}^2$
A	0.53	8.25	386	$3.16 \cdot 10^6$	$3.67 \cdot 10^6$	$3.79 \cdot 10^6$	$5.94 \cdot 10^6$
B	1.61	8.35	396	$2.74 \cdot 10^6$	$3.72 \cdot 10^6$	$3.81 \cdot 10^6$	$5.89 \cdot 10^6$
C	2.12	8.5	393	$3.75 \cdot 10^6$	$4.43 \cdot 10^6$	$4.02 \cdot 10^6$	$6.11 \cdot 10^6$
D	3.07	8.35	398	$3.06 \cdot 10^6$	$3.66 \cdot 10^6$	$3.79 \cdot 10^6$	$5.87 \cdot 10^6$
E	4.04	8.35	402	$2.52 \cdot 10^6$	$3.16 \cdot 10^6$	$3.75 \cdot 10^6$	$5.8 \cdot 10^6$
F	5.15	8.35	427	$2.28 \cdot 10^6$	$2.57 \cdot 10^6$	$3.54 \cdot 10^6$	$5.47 \cdot 10^6$

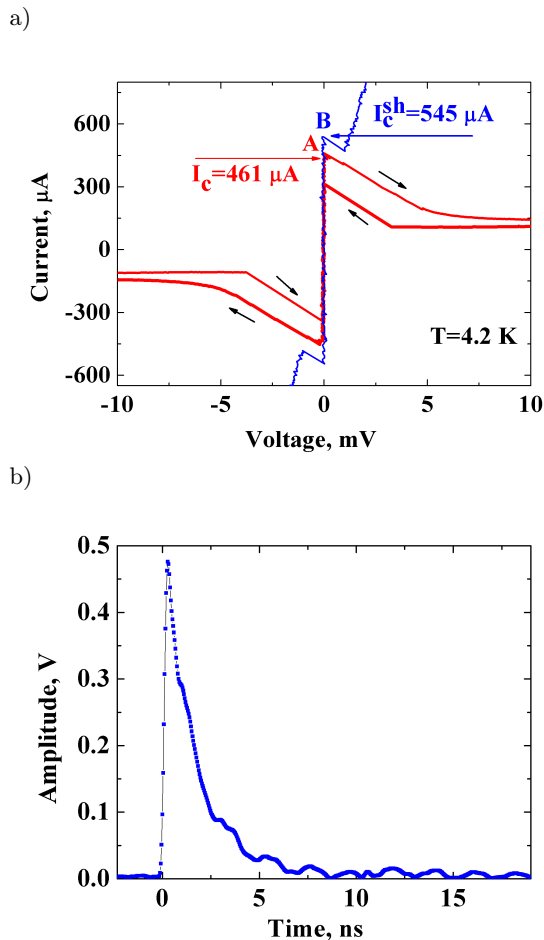


FIG. 2. (a) I-V curves of Sample C measured with  $3\Omega$  shunt resistor (blue) and without (red) at temperature  $T=4.2$  K. (b) Single-shot waveform transient from Sample C when a photon is absorbed.

In applying these expressions to the present NbN films we make a conceptual step, which would require a deeper justification, and which is currently not available. It is known that the critical temperature  $T_c$  varies with the resistance per square, reminiscent of experiments on the

superconductor-insulator transition [9, 22–25]. It has also been found that the ratio of  $\Delta(0)/k_B T_c$  for such films is not a constant but changes with the resistance per square. It is often attributed to the film properties and the substrate surface [26]. Nevertheless, there is compelling evidence that these materials are anomalous in many respects [27]. Given this uncertainty we make the choice to take the most straightforward input towards Eqs.(1,2) and we use the BCS ratio for  $\Delta$  and  $k_B T_c$  and for  $k_F l \approx 3-5$  [23, 25, 26, 28]. For the diffusion constant we use  $D=0.31 \text{ cm}^2/\text{s}$  determined from the upper critical field (see more detail on Sample C in Appendix A). Similarly, we use Eq.2 together with the temperature dependence expressed in Eq.1 as a best estimate for the theoretical depairing current. For further study, we selected the samples with the highest ratio of  $j_c/j_{dep}$  to analyse the photon response.

Biased near the critical current we observe voltage pulses quite similar to those we routinely observe with the usual meander-type SSPD's. Fig. 2(b) presents a typical voltage transient of the  $2.12\text{-}\mu\text{m}$ -wide bridge. The decay time is much shorter than in the meandering SSPDs, but it is still longer than expected from the kinetic inductance  $L_k$  of the bridge [29] connected to the  $3\text{-}\Omega$  shunt resistor. The value of  $L_k$  in our samples is in the range of  $0.4$  to  $1.1 \text{ nH}$ , giving a characteristic decay time in the sub-nanosecond range. We attribute this discrepancy to a parasitic inductance of the read-out lines and the mounting.

### III. SINGLE PHOTON DETECTION

The photon-detection has been carried out in an experimental set-up discussed in detail in Appendix B. Fig. 3 presents real-time waveform transients taken by a digital oscilloscope. The top blue curve shows the clock pulses from the laser. All the other red curves are the responses from the sample measured for decreasing power, by increasing the optical attenuation. We observe: (1) the amplitude of the photoresponse does not depend on the attenuation, and (2) the probability to observe a response

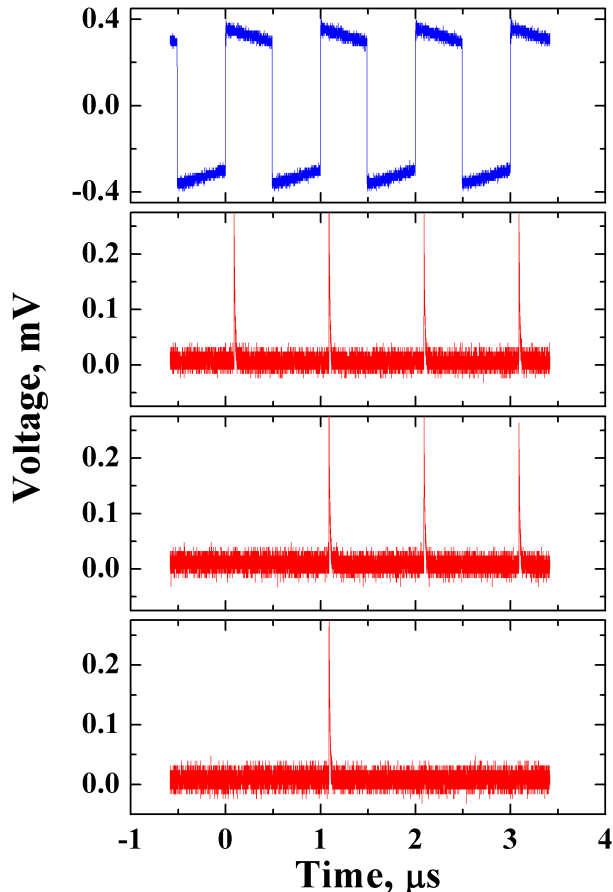


FIG. 3. Real-time waveform record showing clock pulses from the laser (top blue) and photon pulses detected by the bridge at different attenuation levels of the power from the laser (red curves, power decreases from top to bottom). With the increase of attenuation of the power the number of detected pulses decreases.

drops with the increase of optical attenuation.

We proceed with a statistical analysis of the photon count rate on the number of incident photons used previously in Refs. 30, 31. In the single-photon counting regime the photon count rate  $R$  should be proportional to the photon flux  $R_{ph}$ :  $R \propto R_{ph}$ . For multi-photon detection we expect that  $R \propto R_{ph}^n$ , with  $n$  the number of simultaneously absorbed photons producing a single count. This behavior follows from the Poisson distribution of the incident photon-flux. In a strongly attenuated laser beam the probability  $p$  to have a given number of photons  $n$  in a given constant timeslot should be distributed according to:  $p \propto \langle m \rangle^n \exp(-\langle m \rangle) / n!$ , where  $\langle m \rangle$  is the mean number of photons in the timeslot. The probability  $p$  of detecting one photon is proportional to the mean photon number  $\langle m \rangle$ , the probability of detecting two photons is proportional  $\langle m \rangle^2$ , and so on. In Fig. 4 we show the count rate *vs* incident photon flux for Sample C

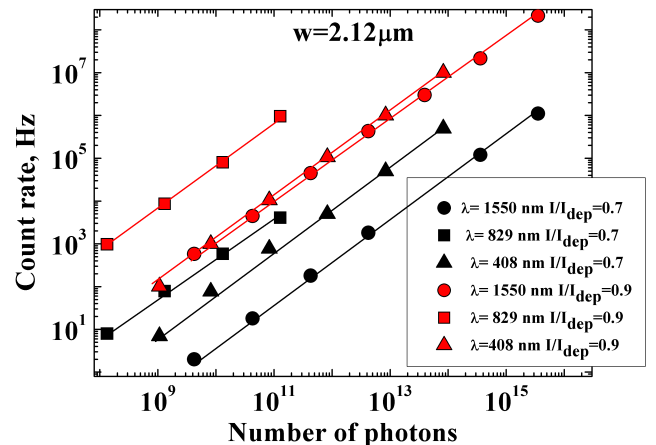


FIG. 4. Count rate *versus* the number of photons in the laser pulse. Blue symbols for  $I_{bias} = 0.7I/I_{dep}$ , red symbols for  $I_{bias} = 0.9I/I_{dep}$ . The linear dependence of the count rate with the number of photons in the pulse corresponds to the Poisson statistics and indicates the single-photon nature of the response, irrespective of the bias current.

at three wavelengths: 408 nm, 829 nm and 1550 nm and for 2 bias currents. We selected two bias currents which are supposed to correspond to two different mechanisms of photoresponse as proposed by Zotova and Vodolazov [15]: (1) *Regime I* (at  $I_{bias} = 0.5I/I_{dep}$ ) corresponds to the initial sharp increase of the IDE and (2) *Regime II* (at  $I_{bias} = 0.78I/I_{dep}$ ) denotes a much slower increase of IDE. More details about these regimes will be given below. One can see that for all studied wavelengths and bias currents we observe  $\propto R_{ph}$ , a dependence which confirms the single-photon operation of the sample. We observe the same results for all studied samples including the largest 5-15  $\mu\text{m}$ -wide Sample F.

As a further test of the response we studied inter-arrival time distribution of photon counts as suggested by Marsili et al [32]. The statistics of inter-arrival time is studied using the digital oscilloscope Tektronix DPO-70404C. We record the waveform-transient of maximum length, which is a total of 12.5 million points, covering 10 ms windows with 800 ps resolution. Such a time resolution made it possible to obtain at least one point on the rising edge and 2-3 points on the decreasing edge of the pulse (Fig. 5(a)). As a result we have a set of times  $t_i$  and, correspondingly, the instantaneous voltages  $U_i$ . Then, we extract all time-moments  $t_{iA}$ , which correspond to the appearance of photo-counts. As an objective criterion, we took the voltage rise above a threshold value, to indicate the voltage pulses  $U_{iA}$ , which count as events.  $U_{iA}$  is taken much larger than the noise amplitude. From the array  $t_{iA}$  we determine the time intervals between all successive photo-counts:  $\Delta t_i = t_{i+1} - t_i$ . From this we construct a histogram of the distribution of these time intervals, normalized to the number of time intervals and their width. Fig. 5(b) shows the histograms of this inter-

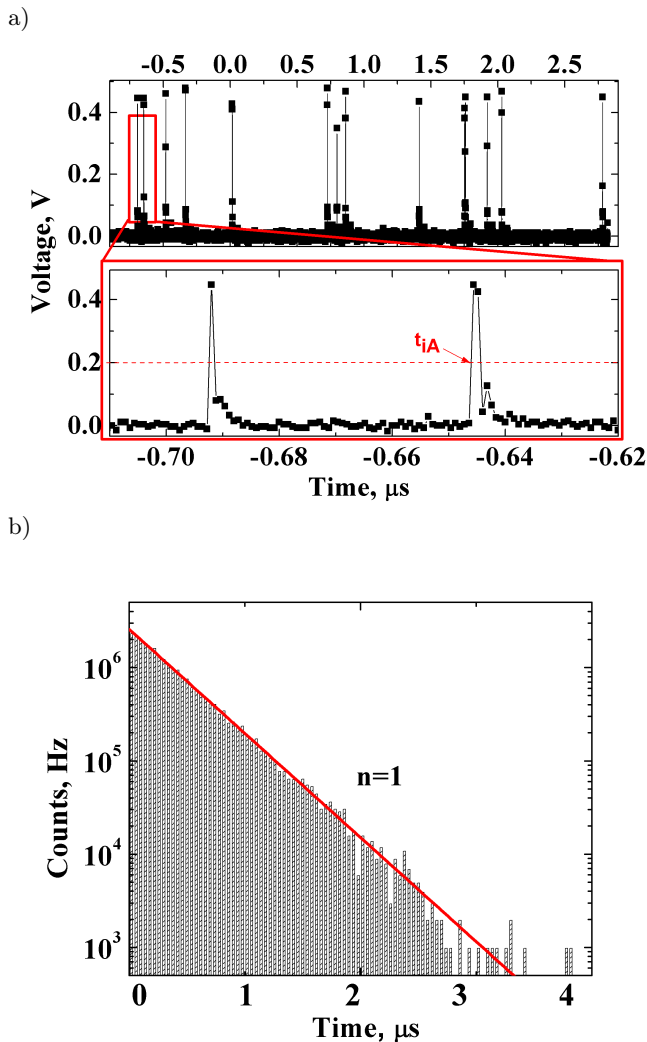


FIG. 5. (a) Oscilloscope waveform transient (top) and a fragment of the timetrace (bottom). (b) Statistical analysis of the inter-arrival time of the photon counts measured with cw laser of wavelength  $\lambda=1550$  nm. The exponential distribution of the inter-arrival time intervals between photon counts shows the same Poisson distribution as for the photons in the incoming light providing additional proof of the single-photon response of the sample.

arrival time for Sample D.

Since the photons in the incoming light from the cw laser are independent and since they obey Poisson statistics, the probability to record  $n$  photons in a time interval  $t$  is  $(\nu t)^n \exp(-\nu t)/n!$ , with  $\nu$  the mean photon flux. Let the first count being observed at  $t = 0$ . The probability of a second count during the interval from  $t$  to  $t + dt$  is the multiplication of probabilities to have exactly one photon in the interval  $[t, t + dt]$  and  $n - 1$  photons in  $[0, t]$ . The probability of the former event is  $\nu dt$ , the latter is  $(\nu t)^{n-1} \exp(-\nu t)/(n - 1)!$ . Thus, the probability

distribution for the second photon count appearance is:

$$\rho(t) = \frac{\nu(\nu t)^{n-1} \exp(-\nu t)}{(n - 1)!} \quad (3)$$

The red straight line in Fig.5 is the prediction of Eq.3 with  $n = 1$  ( $n$  is number of photons for a time interval  $t$ ). It clearly proves that the sample does not accumulate more than one photon to produce a single photon count.

#### IV. DEPENDENCE OF DETECTION EFFICIENCY ON CURRENT

In Fig. 6(a,b) we show the evolution of the internal detection efficiency  $IDE$  with bias current. We distinguish two regimes, indicated in the figure. In *Regime I* the  $IDE$  grows fast in an exponential-like manner. This *Regime I* we associate with fluctuation assisted photon counting. In this case, the absorption of a photon triggers the transition to the resistive state only with the help of thermally activated vortex nucleation near the point of impact of the photon [15]. The indirect proof of this intrinsic mechanism comes from the fact that the slopes of  $IDE(I)$  in *Regime I* and the dependence of the dark count rate on bias current (see Fig. 6(a,b)) are identical for all samples and bias conditions.

The second regime, *Regime II*, begins at a current denoted by  $I \gtrsim I_2$ , which we relate to the position-dependent photon counting proposed in Refs. 8, 15, 33. In this deterministic regime, the  $IDE$  monotonically grows with the current, starting from the current called  $I_{det}^{min}$ , where the region near the edges of the sample (with typical width about the diameter of the hot spot) starts to detect photons. It grows up to a current  $I_{det}^{max}$ , at which the central part of the sample joins the detection process. For relatively narrow widths it is expected that  $I_{det}^{min} \simeq I_{det}^{max} - 0.1I_{dep}$  (see Fig. 9 in Ref 8). The calculations for wider samples give  $I_{det}^{min} \simeq I_{det}^{max} - 0.03 \div 0.04I_{dep}$  and dependence  $IDE(I)$  has step like form with  $IDE \ll 1$  for  $I < I_{det}^{min}$  and  $IDE = 1$  at  $I > I_{det}^{max}$  due to small contribution of near-edge region of the sample to full intrinsic detection efficiency. Therefore we can safely assume that current  $I_2 \sim I_{det}^{max}$ .

The model of Ref. [8] predicts that the ratio  $I_{det}^{max}/I_{dep}$  increases at higher temperatures (see Fig.11 in Appendix C) and so does  $I_2/I_{dep}$ . This result qualitatively coincides with the present experimental findings. At  $T=4.2\text{K} \simeq 0.5T_c$  ratio  $I_2/I_{dep}$  has a larger value for all the bridges than at  $T=1.7\text{K} \simeq 0.2T_c$ , but the deterministic regime extends over a wider current interval at lower temperatures. Moreover, for example Sample F ( $w = 5.15\mu\text{m}$ ) with the lowest reduced critical current at  $T=4.2\text{K}$ , detects photons at high temperature only in the fluctuation assisted regime, while at  $T=1.7\text{K}$  it operates in the deterministic regime too.

In our experiment *Regime II* extends over the current range  $\sim 0.1 - 0.3I_{dep}$  (depending on the temperature and



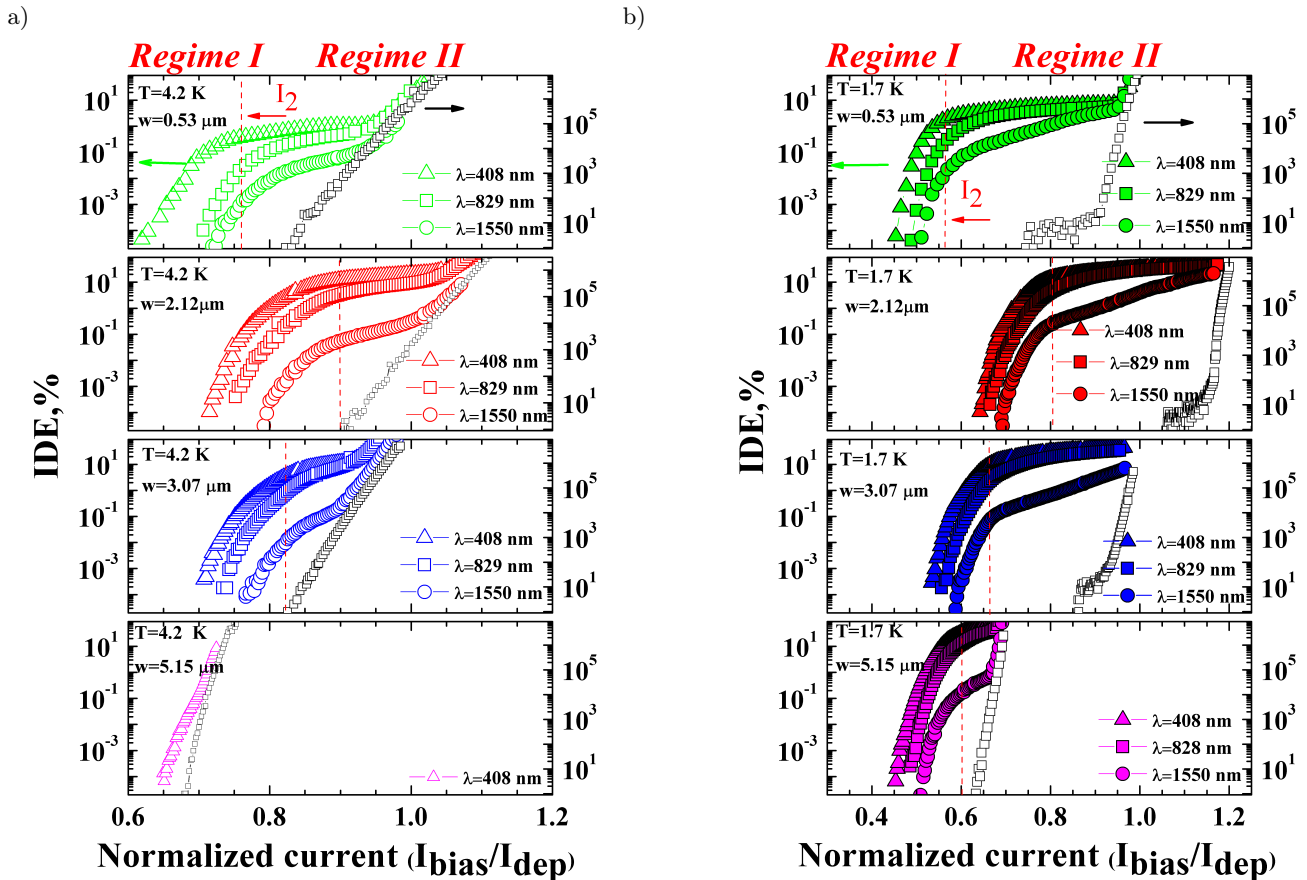


FIG. 6. Dependence of detection efficiency on bias current normalized to the absorption,  $IDE(I)$ . The bias-current  $I_{bias}$  is normalized to the calculated depairing current  $I_{dep}$ . (a)  $IDE$  at 4.2K and (b)  $IDE$  at 1.7K for the Samples (from top to bottom) *A* with  $w=0,53\ \mu\text{m}$  (green symbols), *C* with  $w=2,12\ \mu\text{m}$  (red symbols), *D* with  $w=3,07\ \mu\text{m}$  (blue symbols) and *F* with  $w=5,15\ \mu\text{m}$  (magenta symbols). These dependencies show two regimes: (1) with a sharp increase of the  $IDE$  (*Regime I*) and (2) with a much slower increase of the  $IDE$  (*Regime II*).

the specific sample), which is much larger than the theory [8] predicts. We also do not observe a saturation of  $IDE$ . We believe that the main reason is the geometry of our bridges, Fig. 1. The width of the bridge increases when one moves from its center to the leads and the local current density decreases. Therefore with increasing current a larger (longer) part of the bridge participates in the detection process and the  $IDE$  grows monotonically until the bridge switches to the resistive state at  $I > I_c^{sh}$ .

## V. DISCUSSION

Now, we summarize and explain our observations by using the concept of vortex-assisted detection, introduced by Zotova and Vodolazov [7, 8, 15]. Because our samples have widths large compared to the estimated hot spot diameter and to the coherence length, one expects that the detection mechanism should be insensitive to the width of the bridge, and only dependent on the supercurrent density  $j$ .

The model has one specific prediction. For sufficiently large width of the bridge, the onset of deterministic detection is governed by the current density rather than by the current. Physically, this means that the registration of a detection event, which starts upon exceeding the critical current density (the critical supervelocity) [7, 15], is sensitive only to the local density of the current (and to the size and 'depth' of the spot, determined by the energy of absorbed photon), but not to the distance between the hot-spot and the edge of the strip. The latter requirement is only true if the strip is sufficiently wide, compared to the size of the hot spot.

What sufficiently wide means, is seen in Fig. 11 of Appendix C where the normalized detection current  $I_{det}^{max}/I_{dep}$ , which is proportional to the density  $j_{det}$ , saturates near  $w = 100\xi$ . In our experiment, for most of the samples  $w > 100\xi$  holds, and we identify  $I_{det}^{max}$  with *Regime II* with onset current  $I_2$ . Hence, the density of this current  $I_2/w = j_{det}$  for a given wavelength is predicted to be the same for all the samples (excluding maybe the narrowest sample *A* with a width of the order

of  $100 \xi$  which is a borderline-case).

A direct check of this prediction needs to take into account the following two aspects. 1) there is some on-chip resistance in series with the superconducting bridge, and 2) there is the shunt resistance connected in parallel to the chip. Therefore, we do not know the current, flowing *through the bridge*, with sufficient accuracy. Hence, in the raw data in Fig. 6, one observes a spread of *measured* normalized detection currents  $I_2/I_{dep}$  over the different samples.

However, we find that the results for different samples are unaffected by the wavelength of detected photons, despite of the fact we have sample to sample variations and an uncertainty in the the division of the current between the superconductor and the shunt. This means that the ratio of the detection currents, *even those measured with shunt*, corresponding to two wavelength,  $I_2(\lambda_1)/I_2(\lambda_2)$ , should be the same for all samples with different widths. This prediction can be checked by renormalizing the bias current for all samples by dividing  $I_2$  by the width  $w$ . This value should be the same for one wavelength. After this re-normalization, we expect that  $I_2/w$  at other wavelengths will also be the same for all samples.

Fig. 7 a) demonstrates these results for a temperature of 1.7 K. We normalized the bias currents to match  $IDE(I)$  at  $IDE = 1\%$  for the wavelength of 408 nm. To relate the numbers to the current density, we apply the following procedure. We take the data for Sample B, which has values closest to the critical current measured with and without shunt, hence presumably the lowest on-chip serial resistance. We then calculate the current flowing through the superconducting bridge by multiplying the measured current to the ratio  $I_c/I_c^{sh}$  for this sample, and then divide by  $I_{dep}$  at 1.7 K to obtain the ratio  $j/j_{dep} = I/I_{dep}$ . One can clearly observe that the detection current densities become very close to the wavelength of 829 nm. This holds also for the wavelengths of 637 nm and 937 nm, not shown here. The only deviating sample is the narrowest Sample A, which is in line with the observations above. One can also notice that for the largest wavelength of 1550 nm the variation of the detection current density is significantly worse, which we relate to the breakdown of the pure deterministic detection at low energies of photons.

The same argument about the dependence of  $IDE$  on  $j$  rather than on  $I$  holds also for fluctuation-assisted detection. In this case, one assumes that the detection events in this regime occur in the narrowest part of the bridge with the highest current density. This is also consistent with the data.

Next, for wide strips of constant width, the deterministic nature of detection should result in a step-like dependence of  $IDE$  in its dependence on  $j$ .  $IDE \ll 1$  at  $j < j_{det}$  and  $IDE = 1$  at  $j > j_{det}$ . For our neck-shaped samples, we assume that we have unit probability of response to the absorbed photon in the central part of bridge, where  $j > j_{det}$ . The probability is zero further away from the narrowest part (see inset on Fig.

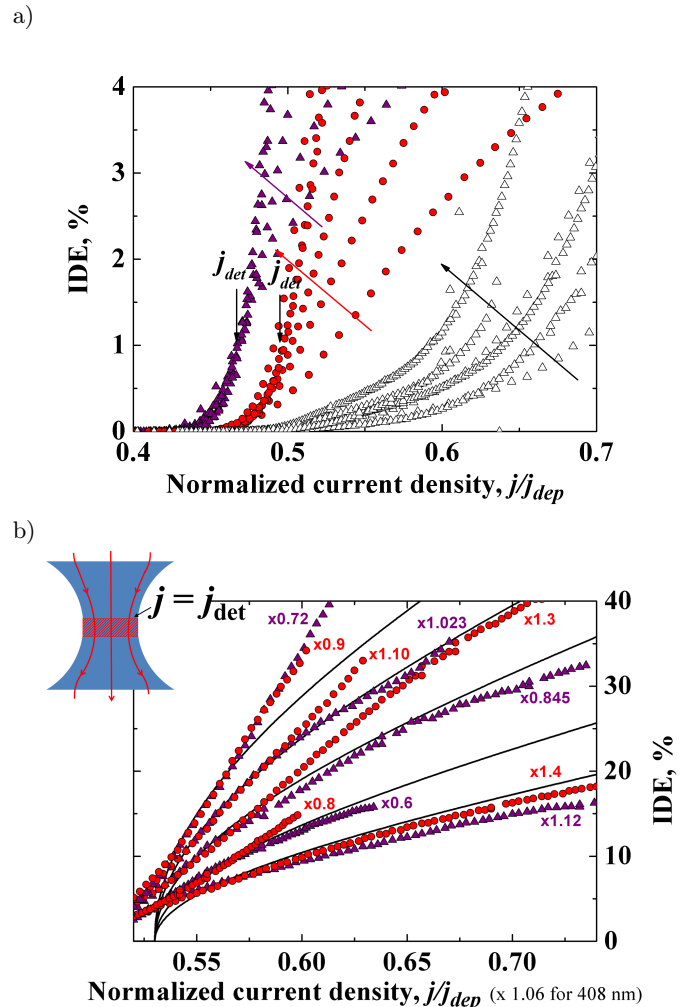


FIG. 7. (a) Dependencies of  $IDE$  on current density near the on-set of *Regime II*, demonstrating invariance of detection current density  $j_{det}$  with respect to the width of the bridge. Violet, red and empty black symbols correspond to the wavelengths of 408 nm, 829 nm and 1550 nm. Widths of the samples are  $w=0,53 \mu\text{m}$  (Sample A),  $1,06 \mu\text{m}$ ,  $1,61 \mu\text{m}$ , (Sample B)  $2,12 \mu\text{m}$  (C),  $3,07 \mu\text{m}$  (D)  $4,07 \mu\text{m}$  (E) and  $5,15 \mu\text{m}$  (F). Arrows show how they correspond to the curves, from narrow to wide. The temperature is 1.7 K. (b)  $IDE$  in the *Regime II* for the wavelength of 408 nm and 829 nm, compared to ratio of detecting area of bridge to its total area. Data for samples C - F is shown, from bottom to top. The temperature is 1.7 K. Inset: schematics of bridge biased by a supercurrent. The part of the bridge, at which  $j > j_{det}$ , detects all absorbed photons, the outer part with  $j < j_{det}$  does not.

7). The boundary between the inner and outer parts is set by the condition  $j = j_{det}$ . Hence, introducing the area of the central, 'detecting', part  $S_{det}(j)$ , we derive the prediction that the internal detection efficiency is  $IDE(j) = S_{det}(j)/S$ , where  $S$  is the total area of the bridge. (The details on calculation of this  $IDE(j)$  can be found in the Appendix D). Fig. Fig. 7 b) compares this prediction with the experiment for the wavelengths



of 408 nm and 829 nm. One sees that the model reproduces the three features: i) steeper increase of  $IDE(j)$  for wider bridges, ii) convex shape of the  $IDE(j)$  dependencies, and iii) up to a factor of 0.7 - 1.5, the absolute value of measured  $IDE$ . The last discrepancy can be explained by systematic and stochastic errors of our method of determination of  $IDE$ . The non-regular deviation of the curves for some of the samples from the model prediction can be attributed to defects in the samples. The model agrees with the experiment qualitatively, and, even quantitatively for a sizable fraction of the samples. This is a strong indication that we observe photon detection with near-unity intrinsic probability at the short wavelengths.

Comparing these findings to the predictions of the microscopic theory, we note that the observed detection current density  $j_{det} \approx 0.5j_{dep}$  for the wavelength of 408 nm is close to the calculated one 8. As expected,  $j_{det}$  increases with the wavelength (*i.e.* with the decrease of photon energy) and appears to equal the experimental  $j_c \approx 0.7j_{dep}$  for the wavelength of 1550 nm. This means that, to realize IDE close to unity for near-IR photons, one has to reach either a larger  $j_c/j_{dep}$ , or, which seems more achievable, to enhance the effect of the hot spot, created by IR photon, on the current density, using thinner films.

## VI. CONCLUSION

We have developed single photon detectors based on NbN microbridges. The dependence of the Internal Detection Efficiency ( $IDE$ ) on the supercurrent qualitatively resembles those of meander-type single photon detectors (SSPDs), with widths less than 200 nm. Our results demonstrate a new type of single photon detector based on a short superconducting bridge with dimensions comparable to the diameter of an optical fiber and an IDE of about one. This design provides a much shorter dead time, which is in the presently used detectors several nanoseconds, due to the long length of the meander-type nanowire. Indirectly our results confirm the vortex assisted mechanism of photon detection by wide current-carrying strip as originally proposed by one of the authors [8].

### Appendix A: Device fabrication and characterization

The 5.8 nm-thick NbN film is deposited by dc magnetron sputtering of a niobium target in a plasma consisting of a mixture of argon (Ar) and nitrogen ( $N_2$ ). The film is deposited on a silicon wafer with a buffer layer of silicon dioxide. The  $SiO_2$  layer is 250 nm-thick. Before starting the sputtering process the substrate is heated to 400°C. The film is characterized by critical temperature of approximately  $T_c=8.3$  K. The deposition is done in the gas mixture with flow rates  $40\text{ cm}^3/\text{s}$  and  $6.6\text{ cm}^3/\text{s}$  for

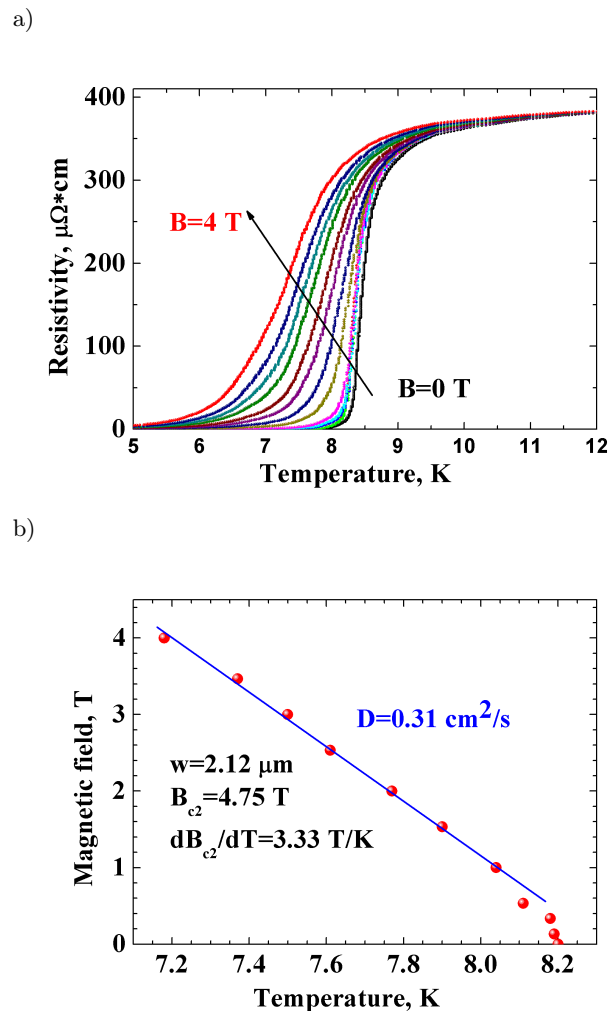


FIG. 8. (a) Dependence of resistivity on temperature for 2.12- $\mu\text{m}$ -wide Sample  $C$  at different magnetic fields in the range from  $B=0$  T to  $B=4$  T. The black arrow indicates the direction of increasing  $B$ . (b) Measured temperature dependence of the critical magnetic field for a 2.12- $\mu\text{m}$ -wide Sample  $C$  (circles), and linear fits of the data (solid line) used for  $B_{c2}(0)$  and the determination of the diffusivity.

Ar and  $N_2$ , respectively, and a current of 550 mA. The deposition rate under these conditions is  $0.88 \text{ \AA}/\text{s}$ .

The NbN film is patterned into single bridge with rounded edges, using the electron-beam lithography and reactive ion etching technique. From one film we make a batch of samples with different widths in the range from  $0.53 \mu\text{m}$  to  $5.15 \mu\text{m}$ . The size of each sample is determined with a SEM. All bridges are characterized by the critical temperature determined from superconducting transition. The I-V curves are determined at temperatures of  $T=4.2$  K and  $T=1.7$  K. From a measurement of the temperature dependence of the second critical magnetic field  $B_{c2}$ , we infer a diffusion constant  $D=0.31 \text{ cm}^2/\text{s}$ , Fig. 8. This value is determined for one device and assumed to be identical for the other devices.

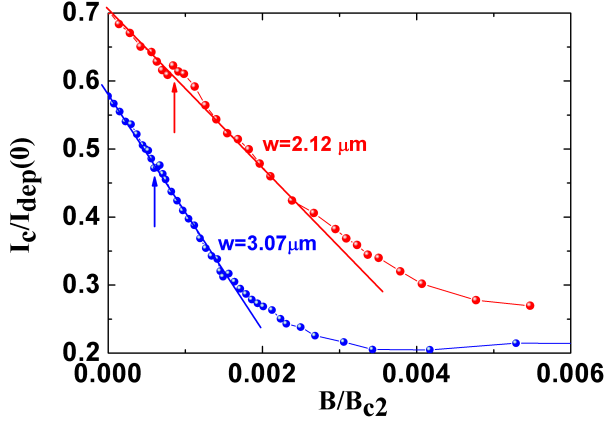


FIG. 9. Dependence of the normalized critical current  $I_c/I_{dep}(0)$  (without the shunt) on the magnetic field measured for 2-12 and 3-07  $\mu\text{m}$ -wide samples. Linear dependence in low magnetic fields is evidence that the NbN film does not have large extrinsic defects leading to vortex-pinning in the strip. The arrow-marked kinks are connected with the appearance of the single vortex chain in the middle of the bridge at that specific magnetic field strength.

Based on experiments on similar samples [34], we expect that this causes an error of at most 20%. Extrapolating the linear temperature dependence of  $B_{c2}$  near  $T_c$  to  $T = 0$  we find  $B_{c2}(0) = 4.75$  T.

As an additional proof of high quality of our bridges we measure dependence of critical current  $I_c$  on perpendicular magnetic field  $B$ . Fig. 9 shows dependencies of  $I_c$  on  $B$  measured for devices  $C$  and  $D$  (2.12- and 3.07- $\mu\text{m}$ -wide). We find the linear decay  $I_c(B)$  at low magnetic field which demonstrates dominant contribution of the edge barrier for vortex entry [35] and kinks in dependence of  $I_c(B)$  at  $B/B_{c2} \approx 10^{-3}$  (marked by arrows) which are connected with the presence of the single vortex chain in the middle of the bridge [36–38]. Both these results could not be observed in the bridge with dominant contribution of bulk pinning to  $I_c$  and presence of large number of defects being able to pin vortices.

## Appendix B: Experimental set-up and measurements

The electro-optical characterization of our samples is performed in a fiber-based set-up. The sample is mounted on a dipstick to be inserted into a liquid He dewar. The measurements are carried out at two temperatures:  $T=4.2$  K and  $T=1.7$  K. The latter is reached by vacuum pumping the helium from a cryo-insert for a storage dewar. As light sources, we use light emitting diodes with wavelengths 408 nm, 637 nm, 829 nm, 937 nm, 1330 nm and 1550 nm which can be operated in both pulsed and cw regimes. The sample-chip with the transmission line is connected to a DC+RF-output port

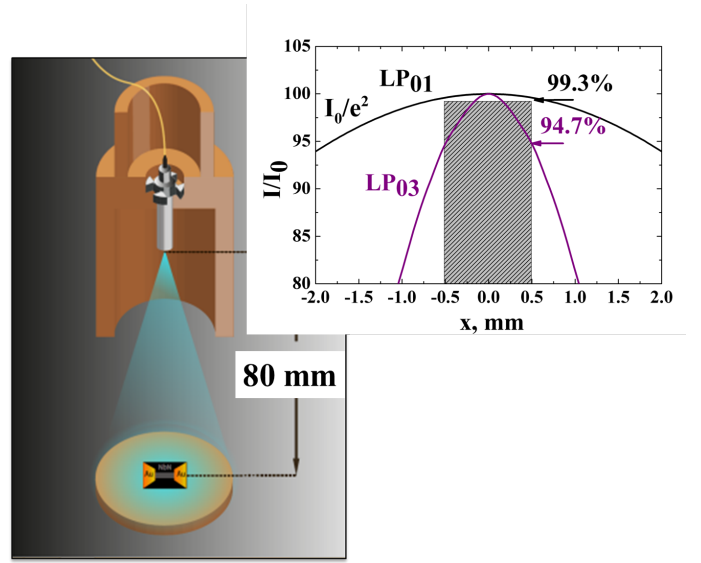


FIG. 10. A sketch of the sample illumination principle: to produce a uniform illumination of relatively large area we place the sample 80 mm away from the fiber pigtail. The insert shows calculation of light beam intensity profile at the sample plane. Curve  $LP_{01}$  is a single-mode profile which is observed in SM-28 fiber for wavelengths longer than 1  $\mu\text{m}$ . It is a Gaussian profile calculated as  $I = I_0 \exp(2x^2/r^2)$ , with  $I_0$  is the irradiance at the center of the beam and  $r_0$  is the radius of the beam at which the irradiance is  $I_0/e^2$  and  $r_0 = d \cdot NA$ , where  $d$  is a distance from surface of optical fiber to surface of detector,  $NA$  is numerical aperture. For fiber SM-28  $r_0 = 11.2$  mm. Curve  $LP_{03}$  corresponds to multi-mode profile at 408 nm wavelength, it is described by Bessel functions of second kind. The gray rectangle corresponds to 0.5 mm displacement, one can see that in the worst case the light intensity is at least 94% of its maximum in the center.

of a bias-T. The bias current is supplied through the DC port. We connect a 3  $\Omega$  resistor in parallel to the sample to prevent latching when the critical current is exceeded. The voltage pulse is amplified by two room-temperature Mini-Circuits ZFL-1000LN+ (1-GHz band, 46-dB total gain) amplifiers, and is fed to a digital oscilloscope and a pulse counter (Agilent 53131A (225 MHz band)).

In view of the topology and the small active area of our samples we do not package them with a single mode fiber as usually done with meander SSPDs [39, 40]. For the present measurements we use the sample holder, shown in Fig. 10. In this sample holder we use the optical fiber SM-28, which is single mode for wavelength 1550 nm with 9  $\mu\text{m}$  core diameter and a NA (numerical aperture) of 0.14. However, at lower cut-off wavelength (below 1260 nm) the mode distribution in SM-28 fiber is not Gaussian, because the fiber becomes multimode [41]. To illuminate our bridge uniformly, we increased the diameter of the output Gaussian beam by placing the sample at a distance of  $d=80$  mm from the end of the fiber. Fig. 10 shows the calculated field profiles emitted from the fiber for the wavelengths 1500 nm and 408 nm. At wavelengths

of 1310 nm and 1550 nm the light intensity within 1-mm-diameter spot is not less than 99% of the light intensity in the center (LP<sub>01</sub> profile shown in Fig. 10). For 408 nm wavelength the mode profile is narrower (LP<sub>03</sub> in Fig. 10), but even in this case if the device is displaced by  $\pm 0.5$  mm the light intensity is not less than 95% of the intensity in the center.

The dipstick is calibrated with a meander-SSPD with a filling factor of 50% (100 nm strip and 100 nm gap). The *IDE* of the meander SSPD has been previously measured by packaging it with single mode fibers. Subsequent measurements of this sample in the dipstick with known Detection Efficiency makes it possible to determine the number of photons in the flow incident on the sample with an area of  $10\mu\text{m}\times 10\mu\text{m}$ . Knowing the ratio of the areas of the meander-shaped SSPD and the bridge we calculate the number of photons incident on the bridge.

### Appendix C: Theoretical estimates

In Fig. 11 we present the calculated dependence of  $I_{det}^{max}/I_{dep}$  on temperature for strips with different widths and two wavelengths. The results are obtained in the framework of the two-temperature hot spot model developed by one of the authors in Ref. 8. The calculations have been carried out at temperatures of  $T \geq 0.35T_c$ , where the numerical procedure convergences well. In this model  $I_{det}^{max}$  is defined as the maximal value of the detection current at which all points across the strip participate in the photon detection (and where the intrinsic detection efficiency reaches unity). The growth of  $I_{det}^{max}/I_{dep}$  with temperature in the range of range 0.35 to  $0.7T_c$  is connected with nonlinear temperature dependence of the electronic and the phonon energies [8]. The growth of  $I_{det}^{max}/I_{dep}$  at temperature  $T \gtrsim 0.7T_c$  for wide strips ( $w > 40\xi_c$ ,  $\xi_c = \sqrt{\hbar D/k_B T_c} \simeq 5.4\text{nm}$  for our bridges) is explained by the rapid drop of  $I_{dep}(T)$ . This leads to a reduced Joule heating in the superconductor when the first vortex-antivortex pair nucleates inside the (non-equilibrium) hot spot and worsens conditions for the appearance of a fully normal domain. This is due to the same reason that  $I_{det}^{max}/I_{dep}$  grows for a strip with  $w = 20\xi_c$  and  $\lambda = 620\text{nm}$  at  $T > 0.85T_c$ . One would expect that with the approach to  $T_c$  photon detection becomes impossible [8] because the normal domain cannot appear in the strip.

In the calculations we assume that the escape time of the nonequilibrium phonons to the substrate  $\tau_{esc}$  is equal to the characteristic time  $\tau_0 \sim 270$  ps. Furthermore that the important parameter  $\gamma = 10$ . Both are typical values for NbN (for the definition of  $\tau_0$  and  $\gamma$ , see Ref. 8). Choosing smaller value of  $\tau_{esc}$  (up to  $0.1\tau_0$ ) does hardly change the obtained dependencies, at least for temperatures  $T < 0.8T_c$  because the time for the nucleation of a normal domain  $\delta t$  [8] does not exceed  $0.1\tau_0$ . At  $T = 0.9T_c$  the time  $\delta t$  approaches  $0.4\tau_0$  for a strip with  $w = 180\xi_c$ .

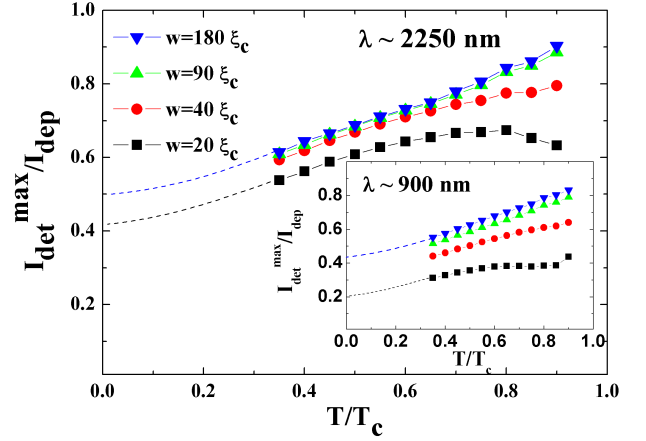


FIG. 11. Dependence of  $I_{det}^{max}/I_{dep}$  on temperature for two wavelengths  $\lambda=2250$  nm and  $\lambda=900$  nm (in insert) of the photon and different widths of the strip. At the current  $I \geq I_{det}^{max}$  all points across the strip participate in photon detection and intrinsic detection efficiency reaches unity. Calculations are made in framework of 2T hot spot model from Ref. 8. Dashed lines show expected dependence at low temperatures (they follow from results for hot belt model – see Fig. 6 in Ref. 8) where numerical scheme from Ref. 8 does not converge.

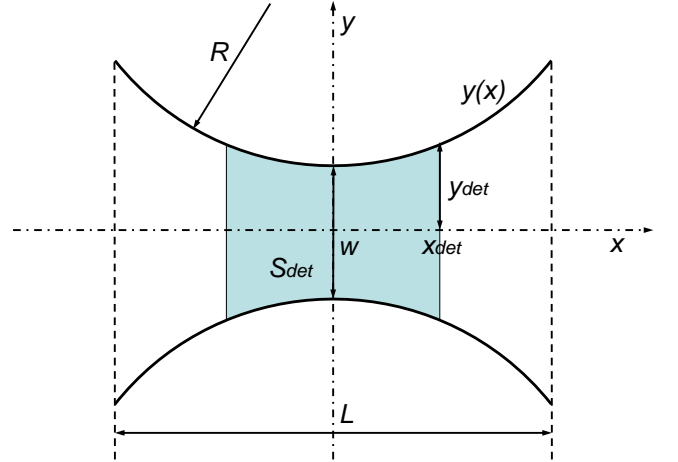


FIG. 12. On calculation of 'detecting' area  $S_{det}$ .

A smaller  $\tau_{esc}$  provides a large value of  $I_{det}^{max}/I_{dep}$ .

### Appendix D: Account for non-rectangular shape of bridges

To apply our simple model of deterministic detection, which predicts  $IDE = 0$  at  $j < j_{det}$  and  $IDE = 1$  at  $j > j_{det}$ , to our bridges with non-constant width and hence non-constant  $j$  over the length, we calculate 'detecting' amount of the bridge area, in which  $j > j_{det}$ . To do it, we introduce coordinates as shown

on Fig. 12. We express area of the bridge segment of length  $2x$  as  $S(x) = 4 \int y(x) dx \approx 2wx + 2x^3/3R$ , where  $y(x) = w/2 + R - \sqrt{R^2 - x^2} \approx w/2 + x^2/2R$  is the half-width of the bridge at the cross-section with the coordinate  $x$ . The current density at the same cross-section is  $j(x) = jw/y(x)$ , with  $j$  the current density at the center of the bridge  $x = 0$ . At the boundary between detecting and non detecting parts  $x_{det}$ , one has  $j(x_{det}) = j_{det}$  and  $y(x_{det}) = (j/j_{det})(w/2)$ . Expressing half-width at this boundary as  $y_{det} \approx Rw\sqrt{j/j_{det} - 1}$  we derive, that the detecting area  $S_{det} = S(x_{det}) \approx R^{1/2}w^{3/2} \left[ 2(j/j_{det} - 1)^{1/2} + (2/3)(j/j_{det} - 1)^{3/2} \right]$ . Fi-

nally, to obtain  $IDE(j) = S_{det}/S$ , we divide  $S_{det}(j)$  to the total area of bridge  $S \approx wL + L^3/12R$ .

## ACKNOWLEDGMENTS

The work is supported by the Russian Science Foundation (RSF) Project No.17-72-30036. TMK is also supported by the European Research Council Advanced grant no. 339306 (METIQUIM).

- 
- [1] C. M. Natarajan, M. G. Tanner, and R. H. Hadfield, *Supercond. Sci. Technol.* **25**, 063001 (2012).
- [2] L. Maingault, M. Tarkhov, I. Florya, A. Semenov, R. E. de Lamaestre, P. C. and G. Goltsman, J.-P. Poizat, and J.-C. Villegier, *J. of Appl. Phys.* **107**, 116103 (2010).
- [3] R. Lusche, A. Semenov, K. Ilin, M. Siegel, Y. Korneeva, A. Trifonov, A. Korneev, G. Gol'tsman, D. Vodolazov, and H.-W. Hübers, *J. Appl. Phys.* **116**, 043906 (2014).
- [4] A. Semenov, G. Gol'tsman, and A. Korneev, *Physica C* **352**, 349 (2001).
- [5] A. Semenov, A. Engel, H.-W. Hübers, K. Il'in, and M. Siegel, *Eur. Phys. J. B* **47**, 495 (2005).
- [6] W. Roger, M. Victor, B. Simon, and T. Francesco, *Superconductors at the Nanoscale* (Walter de Gruyter GmbH, Berlin/Boston, 2017).
- [7] A. N. Zotova and D. . Y. Vodolazov, *Phys. Rev. B* **85**, 024509 (2012).
- [8] D. Y. Vodolazov, *Phys. Rev. Appl.* **7**, 034014 (2017).
- [9] A. Kamlapure, M. Mondal, M. Chand, A. Mishra, J. Jesudasan, V. Bagwe, L. Benfatto, V. Tripathi, and P. Raychaudhuri, *Appl. Phys. Lett.* **96**, 072509 (2010).
- [10] A. Kamlapure, T. Das, S. C. Ganguli, J. B. Parmar, S. Bhattacharyya, and P. Raychaudhuri, *Scient.Rep* **3**, 2979 (2013).
- [11] H. L. Hortensius, E. F. C. Driessen, and T. M. Klapwijk, *IEEE Trans. Appl. Supercon.* **23(3)**, 2200705 (2013).
- [12] J. Romijn, T. M. Klapwijk, M. J. Renne, and J. E. Mooij, *Phys. Rev. B* **26**, 3648 (1982).
- [13] I. Charaev, T. Silbernagel, B. Bachowsky, A. Kuzmin, S. Doerner, K. Ilin, A. Semenov, D. Roditchev, D. Y. Vodolazov, and M. Siegel, *Phys. Rev. B* **96**, 184517 (2017).
- [14] K. Ilin, D. Henrich, Y. Luck, Y. Liang, M. Siegel, and D. Y. Vodolazov, *Phys. Rev. B* **89**, 184511 (2014).
- [15] A. Zotova and D. Y. Vodolazov, *Supercond. Sci. Technol.* **27**, 125001 (2014).
- [16] J. Clem and K. Berggren, *Phys. Rev. B* **84**, 174510 (2011).
- [17] L. G. Aslamazov and A. I. Larkin, *ZhETF Pis. Red* **9**, 150 (1969).
- [18] K. K. Likharev, *Rev. Mod. Phys.* **51**, 101 (1979).
- [19] M. W. Brenner, D. Roy, N. Shah, and A. Bezryadin, *Phys. Rev. B* **85**, 224507 (2012).
- [20] J. Bardeen, *Rev. Mod. Phys.* **34**, 667 (1962).
- [21] J. R. Clem and V. G. Kogan, *Phys. Rev. B* **86**, 174521 (2012).
- [22] Z. Wang, A. Kawakami, Y. Uzawa, and B. Komiyama, *J. Appl. Phys* **79**, 7837 (1996).
- [23] S. Chockalingam, M. Chand, A. Kamlapure, J. Jesudasan, A. Mishra, V. Tripathi, and R. P., *Phys. Rev. B* **79**, 094509 (2009).
- [24] M. Beck, M. Klammer, S. Lang, P. Leiderer, V. Kabanov, G. Goltsman, and J. Demsar, *Phys. Rev. Lett.* **107**, 177007 (2011).
- [25] Y. Noat, V. Cherkez, C. Brun, T. Cren, C. Carbillet, F. Debontridder, K. Ilin, M. Siegel, A. Semenov, H.-W. Hübers, and D. Roditchev, *Phys. Rev. B* **88**, 014503 (2013).
- [26] R. Romestain, B. Delaet, P. Renaud-Goud, I. Wang, J.-C. V. C. Jorel, and J.-P. Poizat, *New J. Phys* **6**, 129 (2004).
- [27] arXiv:1712.07215 [cond-mat.supr-con].
- [28] A. Semenov, B. Günther, U. Böttger, H.-W. Hübers, H. Bartolf, A. Engel, A. Schilling, K. Ilin, M. Siegel, R. Schneider, D. Gerthsen, and N. A. Gippius, *Phys. Rev. B* **80**, 054510 (2009).
- [29] A. Kerman, E. Dauler, W. Keicher, J. Yang, K. Berggren, G. Gol'tsman, and B. Voronov, *Applied Physisc Letters* **88**, 111116 (2006).
- [30] G. Gol'tsman, O. Okunev, G. Chulkova, A. Lipatov, A. Semenov, K. Smirnov, B. Voronov, A. Dzardanov, C. Williams, and R. Sobolewski, *Applied Physics Letters* **79**, 705 (2001).
- [31] Y. Korneeva, I. Florya, S. Vdovichev, M. Moshkova, N. Simonov, N. Kaurova, A. Korneev, and G. Goltsman, *IEEE Trans. on Appl. Supercond.* **27**, 2201504 (2017).
- [32] F. Marsili, F. Najaf, E. Dauler, F. Bellei, X. Hu, M. Csete, R. J. Molnar, and K. K. Berggren, *Nano Lett.* **11(5)**, 2048 (2011).
- [33] A. Engel, J. Lonsky, X. Zhang, and A. Schilling, *IEEE Trans. Appl. Supercond.* **25**, 2200407 (2015).
- [34] M. Shcherbatenko, I. Tretyakova, Y. Lobanov, S. N. Maslennikov, N. Kaurova, M. Finkel, B. Voronov, G. Goltsman, and T. M. Klapwijk, *Applied Physics Letters* **109**, 132602 (2016), <https://doi.org/10.1063/1.4963691>.
- [35] B. L. T. Plourde, D. J. V. Harlingen, D. Y. Vodolazov, R. Besseling, M. B. S. Hesselberth, and P. H. Kes, *Phys. Rev. B* **64**, 014503 (2001).
- [36] V. Shmidt., *Sov. Phys. JETP* **1**, 1054 (1970).
- [37] D. Y. Vodolazov, *Phys. Rev. B* **88**, 014525 (2013).

- [38] K. Ilin, D. Henrich, Y. Luck, Y. Liang, M. Siegel, and D. Y. Vodolazov, *Phys. Rev. B* **89**, 184511 (2014).
- [39] S. Miki, M. Fujiwara, M. Sasaki, and Z. Wang, *IEEE Trans. on Appl. Supercond.* **17**, 285 (2007).
- [40] W. Slysz, M. Wegrzecki, J. Bar, M. Gorska, V. Zwiller, C. Latta, P. Bohi, I. Milostnaya, O. Minaeva, A. Antipov, O. Okunev, A. Korneev, K. Smirnov, B. Voronov, N. Kaurova, G. Gol'tsman, A. Pearlman, A. Cross, I. Komissarov, A. Verevkin, and R. Sobolewski, *Applied Physics Letters* **88**, 261113 (2006).
- [41] J. M. Senior and M. Y. Jamro, *Optical Fiber Communications: Principles and Practice* (Ashford Colour Press Ltd, Gosport, Pearson Education Limited, England, 2009).